Chemical Engineering Journal 166 (2011) 751–764

Contents lists available at ScienceDirect

Chemical Engineering Journal

journal homepage: www.elsevier.com/locate/cej

# Synthesis, thermal behaviour and luminescence properties of rare earth-doped titania nanofibers

Ilaria Cacciotti[a,*], Alessandra Bianco[a], Giuseppe Pezzotti[b], Gualtiero Gusmano[a]

[a] University of Rome "Tor Vergata", Dipartimento di Scienze e Tecnologie Chimiche, INSTM UdR Roma Tor Vergata, Via della Ricerca Scientifica, 00133 Rome, Italy
[b] Ceramic Physics Laboratory & Research Institute for Nanoscience, RIN, Kyoto Institute of Technology, Sakyo-ku, Matsugasaki, 606-8585 Kyoto, Japan

ARTICLE INFO

*Article history:*
Received 3 May 2010
Received in revised form 28 June 2010
Accepted 2 July 2010

*Keywords:*
Titania
Nanofibers
Electrospinning
Scanning electron microscopy
Phase transformations
Luminescence properties

ABSTRACT

Undoped and rare earth (RE = La, Eu and Er)-doped titania nanofibers have been fabricated by electrospinning technique, starting from polyvinylpyrrolidone, titanium tetraisopropoxide ($Ti(OiPr)_4$) and $Eu(NO_3)_3$, $La(NO_3)_3$ and $Er(NO_3)_3$. A systematic microstructural and spectroscopic characterisation of RE-doped $TiO_2$ nanofibers is presented by means of scanning electron microscopy (SEM), thermal analysis (TG–DTA), X-ray diffraction (XRD and HT-XRD) and Raman spectroscopy. Optical properties were investigated both by means of luminescence spectroscopy and by a FEG-SEM, equipped with a cathodoluminescence device. All electrospun materials consisted of randomly oriented nanofibers of fairly uniform diameter. The average fiber size was 40 nm and 40–79 nm for undoped and RE-doped $TiO_2$ calcined at 500 °C, respectively. The progressive lowering of the thermal decomposition temperatures of the PVP matrices upon admixing $TiO_2$ precursor and RE ion sources might be correlated to catalytic properties of both metal centres.

The presence of RE elements shifted toward higher values the anatase to rutile phase transition temperature (up to 900–1000 °C), with the simultaneous formation of the $Ln_2Ti_2O_7$ phase (Ln = Eu, Er). The Raman spectroscopy analysis revealed the typical anatase phase vibrational modes at 500 °C and the rutile phase ones at 1000 °C, accordingly to the XRD phase evaluations. In the case of La-doped sample, luminescence spectra were comparable to those registered for undoped $TiO_2$, suggesting that $La^{3+}$ doping did not cause a new luminescent phenomenon, but affected the response range and intensity. The luminescence spectra of Eu- and Er-doped samples clearly testified the presence of lanthanide ions in the $TiO_2$ host lattice, showing the characteristic transitions of $Ln^{3+}$ ions. The emission spectra were characterised by inhomogeneously broadened bands, suggesting a relevant disorder around the $Ln^{3+}$ sites, typical of $Eu^{3+}$ and $Er^{3+}$ doped systems.



## 1. Introduction

During the recent decades, the photocatalytic application using semiconductors has attracted much interest to solve the environmental problems [1–5]. Titanium dioxide ($TiO_2$) is one of the most studied semiconductors for photocatalytic reactions as catalyst and catalyst support (i.e. for selective catalytic reduction of $NO_x$ with $NH_3$ (SCR process) and hydrogen production by photoelectrolysis, enhancing the efficiency of electrolytic splitting of $H_2O$ into $H_2$ and $O_2$) [6] due to its high photocatalytic activity, low cost, no-toxicity, high stability in aqueous solution and toward photocorrosion, ease of handling, high resistance to photo-induced decomposition [6–8], high light-conversion efficiency and environmental benign properties [9–11]. Moreover, its high photo-degradation efficiency for organic compounds allows its use in the fields of purification and treatment of polluted water and air [12,13].

In recent years, many studies have been focused on the use of $TiO_2$ in applications such as gas sensors [14], waveguides [15], solar energy cells [16] and photo-catalysts [17]. In particular, the photocatalytic properties of titanium dioxide were extensively investigated and these are due to its wide bandgap and long lifetime of photogenerated holes and electrons. However $TiO_2$ has high band gap energy (3.2 eV), which limits its application in visible light range of solar spectrum. A good photocatalyst strongly depends on its efficiency of electron–hole pair separation and its optical absorption property. Thus a key challenge in heterogeneous photocatalysis is to increase the charge separation efficiency of the photocatalysts [18].

In this framework, several investigations are devoted to the modification of microstructures and improvement of reactivity of nanosized $TiO_2$ [19–21]. It has been widely demonstrated that the photocatalytic reactivity of titanium dioxide can critically depend on several factors, including microstructure [22–24], crystal modification, particle size, preparative route, surface area, porosity, thermal history, foreign ions, etc. [19–21,25–28]. In fact, among the common three crystalline forms of titania (anatase, rutile,

* Corresponding author. Tel.: +39 0672594482; fax: +39 0672594328.
*E-mail address:* ilaria.cacciotti@uniroma2.it (I. Cacciotti).

1385-8947/$ – see front matter © 2010 Elsevier B.V. All rights reserved.
doi:10.1016/j.cej.2010.07.008

brookite), anatase is generally recognized to be the most active phase for most photoreaction [29,30]; quantum sized $TiO_2$ powders show much greater photoactivity than their bulk phase due to larger specific surface areas and increased band-gap energy, taking place the reactions on the $TiO_2$ surface [31]. However, unfortunately, nanosized $TiO_2$ undergoes an earlier phase transformation of anatase-to-rutile (A–R) than its bulk phase with a simultaneous great decrement of surface area [32–36]. The phase transformation A–R and the decrease in surface area are serious problems for practical applications of these catalysts without deactivation at high temperatures. Doping $TiO_2$ with impurities such as various inner transition metals [37–43], sulphate [44], etc. has been established to be an efficient route to effectively eliminate the electron–hole recombination in the photocatalytic reaction and to alter both the photoactivity and anatase–rutile phase transformation of titania [33–36]. The identification of the most suitable metal ion dopant appears to be the most important factor in the enhancement of photoreactivity of doped titania [25,45,46]. In particular, $TiO_2$ doped with certain types of transition metals has been extensively studied since these transition metal clusters could elongate electron–hole pair separation [47].

Recently, doping lanthanide into $TiO_2$ has attracted a lot of attention [48–50], because lanthanide ions are known for their ability to form complexes with various Lewis bases (i.e. amines, aldehydes, alcohols, thiols, etc.) in the interaction of these functional groups with the f-orbital of the lanthanides [51,52]. Thus, it is expected that incorporation of lanthanide ions into a $TiO_2$ matrix could provide a means for concentration of the organic pollutant at the semiconductor surface and therefore enhances the photocatalytic activity of the catalyst [53–55]. Moreover, the incorporation of a doping metal into a $TiO_2$ framework can provide more active sites on the surface of the inside channel, and can add acidity, leading to different physicochemical properties as well as improved catalytic behaviour.

Photocatalysts with fiber morphology have caught great attention due to their high surface area, low-pressure drop, short diffusion length, and superior light transport abilities. $TiO_2$ fibers are usually prepared using an impregnation method, which supports titania particles on fibrous materials, such as optical cables [56], glass fibers [57], activated carbon fibers [58], and cellulose fibers [59]. Recently, electrospinning was used to generate $TiO_2$ nanofibers with tailored fiber diameter [60,61]. Electrospinning is a simple and versatile technique for the fabrication of a rich variety of nanofibers from a wide range of materials [62], such as polymers [63], composites [64], ceramics [65], and proteins [66], showing several advantages (production of long and continuous nanofibers, control of fiber diameter, and cost effectiveness). RE-doped $TiO_2$ nanofibers prepared by electrospinning have been rarely investigated. Specifically, $Er^{3+}$-doped $TiO_2$ nanofibers have been studied [67–69] and only few papers report about $Eu^{3+}$-doped $TiO_2$ nanofibers [70–72]. To our knowledge, there is a lack of publications reporting systematic studies dealing with the rare earth doped electrospun titania nanofibers and only one paper was focused on a comparison between electrospun RE-doped PVP-$TiO_2$ nanohybrids prepared using different RE ions [72]. Namely, Wang et al. studied the photoluminescence properties of Eu-, Er-, Ce- and Pr-doped titania nanofibers prepared starting from europium, erbium, cerium and praseodymium acetylacetone precursors [72].

In this framework, we reported a systematic detailed description of thermal behaviour, structural phase transformations, luminescence properties of different lanthanide doped titania nanofibers, starting from rare earth nitrate reagents. Three rare earth metals, europium, lanthanum and erbium, were chosen as dopants with the amounts ranging between 1 and 3 mol%. Titanium tetraisopropoxide ($Ti(OiPr)_4$) and $RE(NO_3)_3$ (RE = Eu, Er and La) have been used as titania precursor and rare earth element sources, respectively. The use of rare earth commercial compounds shows some advantages with respect to metalorganic precursors, in terms of low cost and higher availability, even if they present incorporated residues and impurities and high water content that limits their compatibility and solubility in non-aqueous solution.

The purpose of this work is to more deeply understand the effect of various lanthanide dopants on the thermal stability, the textural characteristics and luminescent properties of $TiO_2$.

In order to pursue this aim, morphology of obtained nanofibers was studied by means of scanning electron microscopy (SEM), thermal behaviour followed by thermogravimetric and differential thermal analysis (TG–DTA), the spectroscopic characterisation carried out at room temperature (RT) using a Raman microprobe spectrometer, phase analysis performed by means of X-ray diffraction (XRD) and high temperature X-ray diffraction analysis (HT-XRD) up to 1100 °C. Luminescence properties were investigated both by means of luminescence spectroscopy upon laser excitation at 488 nm and by a scanning electron microscope FEG-SEM, equipped with a cathodoluminescence (CL) device.

## 2. Experimental

### 2.1. Reagents

Commercial europium nitrate pentahydrate ($Eu(NO_3)_3{\cdot}5H_2O$, MW 428.06), lanthanum nitrate hexahydrate ($La(NO_3)_3{\cdot}6H_2O$, MW 433.01) erbium nitrate pentahydrate ($Er(NO_3)_3{\cdot}5H_2O$, MW 443.35), polyvinylpyrrolidone (PVP, MW 1,300,000) and titanium tetraisopropoxide ($Ti(OiPr)_4$, MW 284.22) were purchased from Aldrich and used without any further purification.

### 2.2. Fabrication of undoped and RE-doped $TiO_2$ nanofibrous mats

Polyvinylpyrrolidone (PVP, Aldrich, MW 1,300,000) solution (7 wt%) was prepared dissolving PVP powder in ethanol at RT under magnetic stirring. Then, $TiO_2$ precursor solution was prepared, mixing 1.5 g of titanium tetraisopropoxide ($Ti(OiPr)_4$, Aldrich) with 3 ml of acetic acid and 3 ml of ethanol and stirring for 10 min. The resulting mixture was added to 7.5 ml of PVP solution previously prepared and stirred for further 10 min.

In the case of rare earth doped $TiO_2$, 1 and 3 mol% (with respect to $Ti(OiPr)_4$) of rare earth nitrate were added to $TiO_2$ precursor solution.

The solution was poured in a glass syringe (*Hamilton*, *Carlo Erba*) equipped with a 21 G needle, fixed in a digitally controlled syringe pump (*KD Scientific*, *MA*, *USA*). The needle was connected to a high-voltage supply (*Spellman*, *Model SL 30*, *NY*, *USA*) that is capable of generating DC voltages up to 30 kV. The solution was electrospun in air in the following conditions: tension 15 kV, needle-target distance 5 cm, feed rate 1 ml/h. Electrospun mats were dried under vacuum for 24 h. The resulting mats were designed as PVP/$TiO_2$:*x*RE (*x* = 1 and 3, RE = Eu, Er and La). Only in the case of lanthanum doping, it was not possible to proceed with the electrospinning of 3 mol% La-doped $TiO_2$ precursor solution. Finally, all electrospun mats were calcined at 500 °C, in order to selectively remove the polymeric component. Furthermore, selected samples were heated at 1000 °C for 3 h.

Besides, both undoped and doped samples have been produced several times and it was verified that a good synthesis reproducibility has been achieved.

### 2.3. Characterisation of undoped and RE-doped $TiO_2$ nanofibrous mats

Viscosity of all polymeric solutions was measured at 25 °C by digital viscosimeter (*Brookfield DV-II+*, *Middleboro*, *MA*, *USA*)

equipped with a SC4-21 spindle at 100 rpm and conductivity measured at 25 °C by conductivitymeter (CDM230, *Analitica De Mori, Italy*).

Morphology of the produced electrospun mats was investigated by Scanning Electron Microscopy technique (FEG-SEM, *SE-4300, Hitachi Co., Tokyo, Japan*), and the average fiber diameter was estimated using ImageJ software (on ~100 fibers selection). Energy Dispersive Spectroscopy (EDS) mappings of Ti and RE elements were perfomed on 24.3 μm × 18.2 μm areas by means of *INCA Energy 300, Oxford ELXII detector*.

X-ray diffraction (XRD) (*Philips X'Pert 1710*) (Cu $K_\alpha$ radiation λ = 1.5405600 Å, 2θ range 10–80°, step size 0.020°, time per step 2 s, scan speed 0.005° $s^{-1}$) measurements were performed on both *as-spun* and calcined (500–1000 °C) mats. Phase evolution of *as-spun* membranes was investigated by high temperature XRD measurements (HT-XRD) (*Anton Paar HTK 1200*) in the following conditions: Cu $K_\alpha$ radiation λ = 1.5405600 Å, 2θ range 10–80°, heating rate 5 °C/min, peak temperature 1100 °C, cooling rate 2 °C/min, dwelling 1 h, step size 0.020°, time per step 2 s, scan speed 0.005° $s^{-1}$. The mass fractions of anatase phase and rutile phase were evaluated, using XRD patterns detected on samples calcined at 900 °C, in terms of the relative intensity of maximum anatase phase peak (1 0 1) and maximum rutile phase peak (1 1 0), as follows:

$$\varpi_A = \frac{I_A}{I_A + 1.265 I_R} \times 100$$

where $\omega_A$ is the content of anatase, $I_A$ the intensity of maximum anatase phase peak (1 0 1) and $I_R$ the intensity of maximum rutile phase peak (1 1 0). The content of rutile phase is $(1-\omega_A)$ $(\omega_R)$ [73].

Cell parameters of pure and RE doped $TiO_2$ mats were estimated through the algorithm *TREOR* (*Philips X'Pert Plus software*).

The thermal behaviour of *as-spun* samples was investigated by simultaneous thermogravimetry and differential thermal analysis (TG-DTA, *Netzsch STA 409*) in the following conditions: sample weight about 30–40 mg, heating rate 5 °C/min, peak temperature 1250 °C.

The spectroscopic characterisation of the *as-spun* and calcined samples was carried out at room temperature (RT) using a Raman microprobe spectrometer (*ISA, T-64000, Horiba Jobin Yvon Inc.*) operating at a wavelength of 488 nm with a power of 100 mW.

The optical properties of the obtained samples were studied either by means of Raman spectroscopy upon laser excitation at 488 nm and by a scanning electron microscope FEG-SEM, equipped with a cathodoluminescence (CL) device. Raman measurements were performed with a Raman microprobe spectrometer (*ISA, T-64000, Horiba Jobin Yvon Inc.*) at room temperature (RT). The 488 nm line of an Ar-ion laser (*Stabilite 2017, Spectra Physics, Mountain View, CA, USA*) was used as the excitation source, with a power of 100 mW. An optical microscope was utilized both to focus the laser on the sample and to collect its scattered signal. Scattered frequencies were analyzed with a single-monochromator equipped with a liquid nitrogen cooled charge-coupled device (CCD) camera. The highest lateral resolution achievable for the laser beam focused on the sample was about 1 mm.

Cathodoluminescence (CL) spectra were excited with a field-emission gun in a conventional scanning electron microscope (FEG-SEM, *SE-4300, Hitachi Co., Tokyo, Japan*), equipped with a high-sensitivity CL detector unit (*MP-32FE, Horiba Ltd., Kyoto, Japan*). The CL experiments were performed at 20 kV and 200 pA of probe current. The emitted CL spectrum was analyzed using a monochromator equipped with a CCD camera. A new mapping device (*PMT R943-02 Select, Horiba Ltd., Kyoto, Japan*) was used and related software was developed to enable collection with nanometer-scale spatial resolution and to automatically analyze large numbers of CL spectra in nearly real time.

**Table 1**
Viscosity and conductivity of PVP solution, undoped PVP/$TiO_2$ and RE-doped PVP/$TiO_2$ precursor solutions.

| Precursor solution | Viscosity (cP) | Conductivity (μS $cm^{-1}$) |
|---|---|---|
| PVP | 68 | 4 ± 1 |
| PVP/$TiO_2$ | 23 | 59 ± 1 |
| PVP/$TiO_2$:1La | 45 | 108 ± 1 |
| PVP/$TiO_2$:3La | 58 | 170 ± 1 |
| PVP/$TiO_2$:1Eu | 56 | 112 ± 1 |
| PVP/$TiO_2$:3Eu | 45 | 250 ± 1 |
| PVP/$TiO_2$:1Er | 54 | 117 ± 1 |
| PVP/$TiO_2$:3Er | 65 | 215 ± 5 |

## 3. Results and discussion

### 3.1. Viscosity and conductivity of undoped and RE-doped precursor solutions

Viscosity and conductivity measurements were performed on all as-prepared electrospinning precursor solutions, playing these characteristics a fundamental role in the control of the morphology and the size of the resulting electrospun fibers [74,75]. The obtained values are reported in Table 1.

Compared to the neat PVP solution, the viscosity of PVP/$TiO_2$ and PVP/$TiO_2$-RE precursor solutions decreased to 25–35 cP *vs.* 68 cP due to the presence of Ti(O*i*Pr)$_4$, as observed and demonstrated otherwise [76]. In the case of the PVP/$TiO_2$-RE precursor solutions the viscosity values ranged between 45 cP (PVP/$TiO_2$:3Eu) and 65 cP (PVP/$TiO_2$:3Er), resulting higher than PVP/$TiO_2$ one, due to the admixture of RE nitrates. The overall electric conductivity in the ceramic spinnable solutions is strongly enhanced when compared to the respective polymeric solutions, in good agreement with Sigmund et al. [65]. Regarding the electric conductivity measurements, the conductivity of the PVP solution was 4 μS $cm^{-1}$, whereas for PVP/$TiO_2$ precursor solution the conductivity remarkably increased up to 59 μS $cm^{-1}$. It has been experimentally verified that this effect has to be attributed to the addition of Ti(O*i*Pr)$_4$ [76].

In the case of RE doped PVP/$TiO_2$ precursor solutions, the conductivity values were further higher than the neat PVP/$TiO_2$ one and increased with the dopant content. In fact, the conductivity values ranged between 108 μS/cm (PVP/$TiO_2$:1La) and 117 μS/cm (PVP/$TiO_2$:1Er) and between 215 μS/cm (PVP/$TiO_2$:3Er) and 250 μS/cm (PVP/$TiO_2$:3Eu) for a RE content of 1 wt% and 3 wt%, respectively.

### 3.2. Morphology of undoped and RE-doped ceramic nanofibers

SEM micrographs (Figs. 1–3) showed that undoped and RE-doped PVP/$TiO_2$ mats, before and after thermal treatments, consisted of defect-free, randomly oriented fibers of fairly uniform diameter. Large interconnected voids were present within the fibers, resulting in a 3D fibrous network.

**Table 2**
Average fiber diameter of undoped and RE-doped PVP/$TiO_2$ mats before and after thermal treatment at 500 °C.

| Sample | Average fiber diameter (nm) | |
|---|---|---|
| | *as spun* | Calcined at 500 °C |
| PVP/$TiO_2$ | 60 ± 15 | 40 ± 10 |
| PVP/$TiO_2$:1La | 55 ± 15 | 40 ± 10 |
| PVP/$TiO_2$:1Eu | 80 ± 50 | 60 ± 10 |
| PVP/$TiO_2$:1Er | 87 ± 55 | 60 ± 15 |
| PVP/$TiO_2$:3Eu | 67 ± 25 | 70 ± 25 |
| PVP/$TiO_2$:3Er | 90 ± 50 | 77 ± 19 |

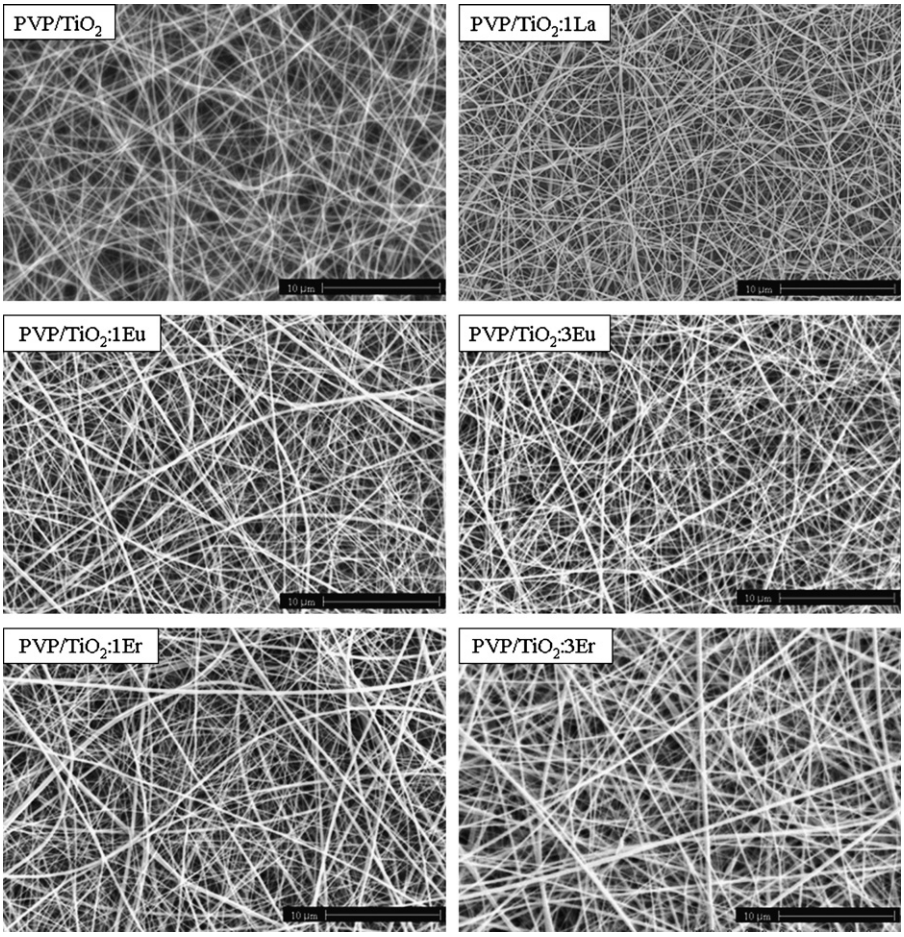


**Fig. 1.** SEM micrographs of *as spun* $PVP/TiO_2$, $PVP/TiO_2$:1La, $PVP/TiO_2$:1Eu, $PVP/TiO_2$:3Eu, $PVP/TiO_2$:1Er and $PVP/TiO_2$:3Er mats.

The average fiber diameter values for all samples are reported in Table 2. The average fiber size of the *as-spun* nanofibers was $60 \pm 15$ nm for the $PVP/TiO_2$ sample (Fig. 1a) and ranged between $55 \pm 15$ nm and $90 \pm 50$ nm for all $PVP/TiO_2$:RE precursor mats (Fig. 1b–f and Table 2). For all $PVP/TiO_2$ materials, a remarkable reduction of fiber size was observed with respect to the neat PVP one ($500 \pm 100$ nm) (not shown), as reported in Ref. [76]. This phenomenon has to be associated with the higher conductivity of the respective solutions (Table 1), being the terminal diameter of the whipping jet controlled by the flow rate, the electric current and the surface tension of the complex fluid [65,77]. Upon thermal treatment at 500 °C, nanosized fibers were obtained having an average diameter of $40 \pm 10$ nm for the neat $TiO_2$ (Fig. 2a) and between $40 \pm 10$ nm and $77 \pm 19$ nm for the RE-doped samples (Fig. 2b–f). It is evident that the nanofibers calcined at 500 °C showed a relatively smooth surface and a random orientation because of the bending instability associated with the spinning jet.

In Fig. 3 the micrographs of sample $TiO_2$:1La calcined at 1000 °C are reported, as an example. After thermal treatment at 1000 °C, the $TiO_2$:RE nanofibers developed a granular microstructure and some of them were cracked. In Fig. 3 it is noticeable that the nanofibers showed burl-like wavy surfaces and consisted of linked crystalline particles or crystallites. This morphology might be related to a dramatic change in crystalline structure.

EDS mappings of RE-doped samples clearly pointed out that Ti and the correspondent RE element were homogeneously distributed throughout the overall samples, as shown in Figs. 2 and 3.

### 3.3. Thermal behaviour of undoped and RE-doped $PVP/TiO_2$ mats

All the electrospun samples were investigated by thermal analyses. In Fig. 4a and b TG–DTA curves of the PVP, $PVP/TiO_2$ and $PVP/TiO_2$:1Eu mats are reported, as an example. All *as spun* mats showed a weight loss around 100 °C related to the removal of physically absorbed moisture and/or of residual solvent (Fig. 4a). The neat PVP underwent a mass loss in the range 300–600 °C corresponding to the PVP combustion and decomposition [42,65,78]. The decomposition of hybrid electrospun $PVP/TiO_2$ mats occurred at lower temperature (i.e. 250–500 °C), further shifted to even lower temperatures in the RE-doped samples. The DTA curves showed the expected exothermic peaks associated with these processes. In particular the exothermic peaks might be ascribed to the Ti–OH decomposition and Ti–O–Ti amorphous network formation (280 °C) and with the PVP decomposition (300–400 °C) (Fig. 4b) [42,79,80]. It is worth observing that the progressive lowering of the thermal decomposition temperatures of the PVP matrices (from 620 °C for neat PVP to 450 °C for the 1% $Eu^{3+}$ doped $PVP/TiO_2$ sample, Fig. 4b) detected upon admixing $TiO_2$ precursor and RE ion sources might be correlated to catalytic properties of both metal centres.

### 3.4. Crystallisation and phase transitions of undoped and RE-doped ceramic nanofibers

High-temperature XRD (HT-XRD) measurements were performed in order to better asses the influence of both the RE dopant

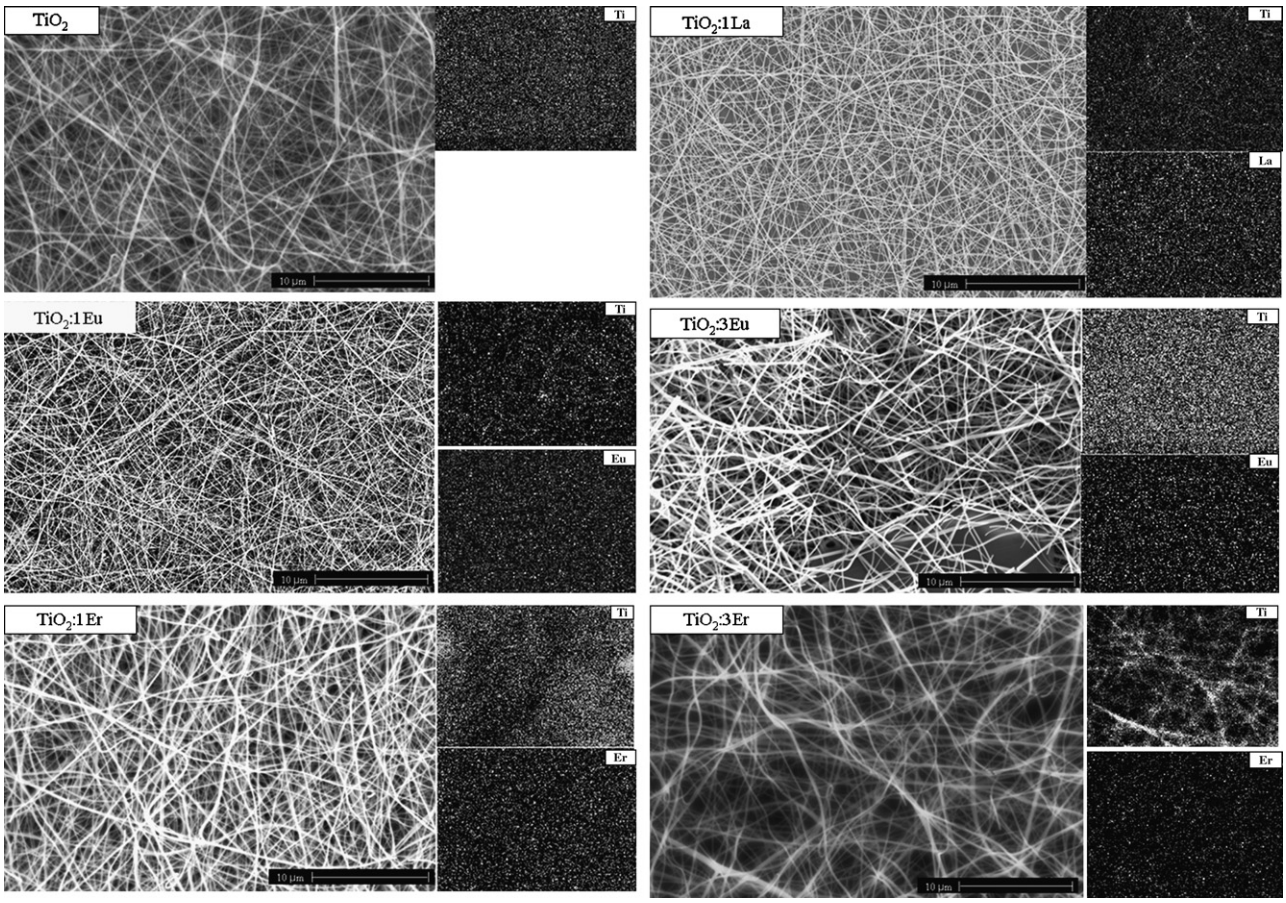


**Fig. 2.** SEM micrographs and EDS mappings of $TiO_2$, $TiO_2$:1La, $TiO_2$:1Eu, $TiO_2$:3Eu, $TiO_2$:1Er and $TiO_2$:3Er electrospun mats calcined at 500 °C.

and the temperature on the crystallisation and the phase evolution. In Figs. 5 and 6 the HT-XRD diffraction patterns of all RE-doped mats are reported.

At first, XRD reflections belonging to lanthanide oxide(s) were not detected in both as-spun and calcined samples. Moreover, a remarkable shift toward higher temperatures of anatase to rutile phase transition with respect to the undoped sample was observed, independently from the dopant ion. In fact, we observed that for undoped $TiO_2$ sample, the crystallisation of anatase phase (JCPDS #84-1286) occurred around 400 °C and the phase transition from anatase phase (JCPDS #84-1286) to rutile phase (JCPDS #73-1765) started at about 600 °C and was completed at around 1000 °C [76].

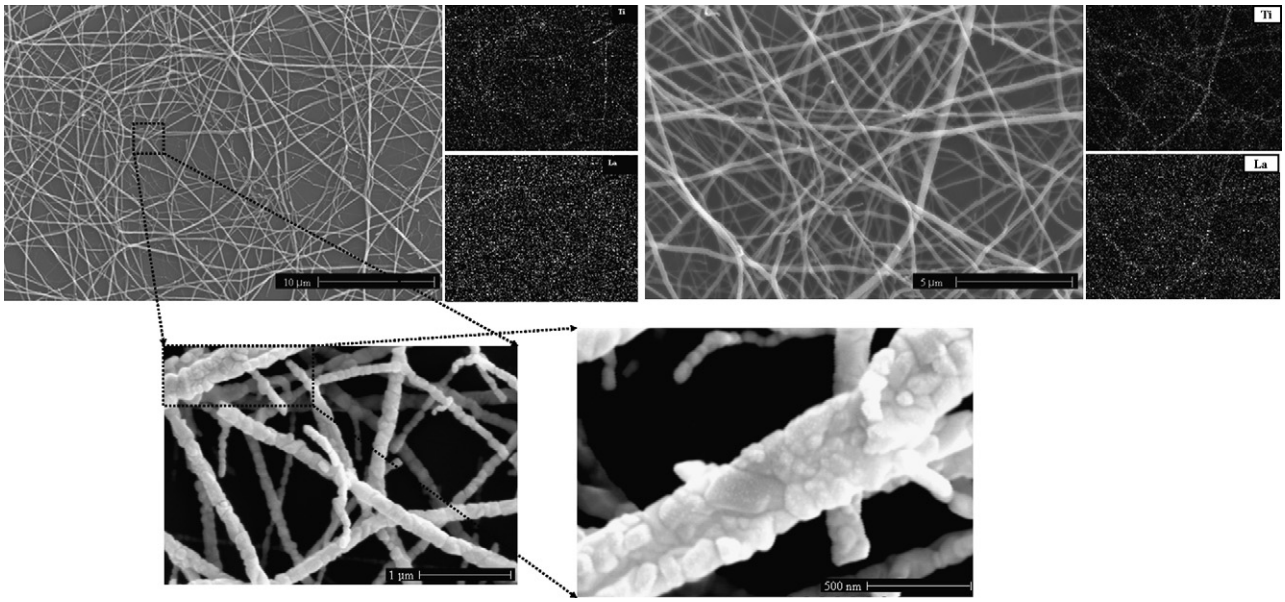


**Fig. 3.** SEM micrographs and EDS mapping of $TiO_2$:1La electrospun mat calcined at 1000 °C.

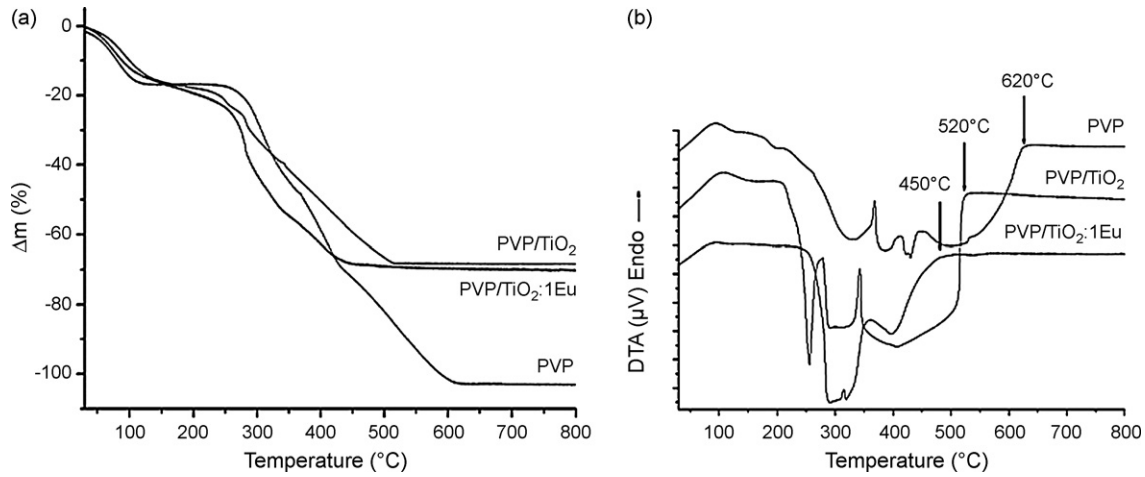


**Fig. 4.** (a) TGA curves of PVP, PVP/$TiO_2$ and PVP/$TiO_2$ Eu doped (1 mol%) electrospun mats, (b) DTA analysis of PVP, PVP/$TiO_2$ and PVP/$TiO_2$ Eu doped (1 mol%) electrospun mats.

In the case of RE-doped samples, the transition anatase to rutile phase was shifted up to 900–1000 °C, depending on the dopant kind and amount. Many authors underlined the effects of rare earth doping on the anatase–rutile (A–R) $TiO_2$ phase transition rates due to perturbation in the crystal nucleation process for the either substitutional or interstitial dopant ion incorporation within host lattice [42,80]. Indeed, the RE ions incorporation within the titania structural framework causes lattice site distortions due to the large difference of ionic radii between $Ti^{4+}$ (0.68 Å) and the specific RE element (1.087 Å for $Eu^{3+}$, 1.040 Å for $La^{3+}$, 1.075 Å for $Er^{3+}$) [42]. Consequently, the nucleation process responsible for the A–R transformation is inhibited by the formation of a Ti–O–RE interaction that segregates the Ti–O species at the interface with the $TiO_2$ domains.

This inhibition effect is supported by the rutile mass fraction ($\omega_R$) values, estimated using XRD spectra of samples calcined at 900 °C. For undoped $TiO_2$ nanofibers, $\omega_R$ was 97%; in the case of doped samples it was remarkably lower (i.e. 3–28%). Moreover, it is worth highlighting that for undoped $TiO_2$, anatase and rutile phases co-existed in a wide temperature range, i.e. from 600 to 900 °C [76]. For RE-doped titania nanofibers, the two polymorphs co-existed only around the transition temperature (900–1000 °C). Besides, by comparing the two different molar RE dopant content, it is evident that in the case of sample doped with Eu, for both $TiO_2$:3Eu and $TiO_2$:1Eu samples the A–R phase transition occurred at about 900 °C (Fig. 6). For Er-doped mats, a significant amount of anatase persisted in samples doped with 3 mol% Er, but the A–R transition occurred at a 100 °C lower temperature (900 °C) than that of 1 mol% one, probably due to the enhancement of defects for high lanthanide content and to the formation of the face centred cubic $Er_2Ti_2O_7$ that promoted the A–R transition (Fig. 6). In fact, increasing the lanthanide content induced a slight decrease in the anatase-to-rutile phase transition. It is likely that the number of defects inside the anatase phase increases with the enhancement of dopant ions and these defects may promote the formation and growth of rutile nuclei [42,80].

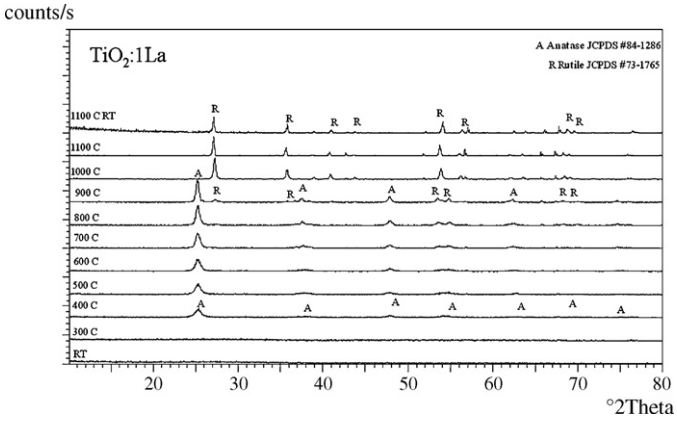


**Fig. 5.** HT-XRD patterns of $TiO_2$:1La electrospun mat (pre-treated at 300 °C) from RT to 1100 °C.

Actually, XRD spectra of both Eu- and Er-doped $TiO_2$ samples showed in the temperature range 900–1000 °C some extra reflections, whose intensity increased with the RE dopant content and with the temperature (Fig. 6). The presence of these peaks could be ascribed to the formation of the face centred cubic $Eu_2Ti_2O_7$ (JCPDS #87-1852) and the face centred cubic $Er_2Ti_2O_7$ (JCPDS #18-0499) (Fig. 6) as secondary phase, for Eu- and Er-doped samples, respectively. Only in the case of $TiO_2$:1La sample, the formation of lanthanum titanate ($La_2Ti_2O_7$) was not observed (Fig. 5), probably due to the low La content. Zhang et al. [42] stated that 1 at.% La-doped nanocrystalline titania showed only rutile phase at 900–1000 °C, without the formation of $La_4Ti_9O_{24}$, which was detected for higher La content (3 and 5 mol%).

As suggested by other authors [42,80], the RE titanate formation is ascribable to enhancement of defects for high lanthanide content. It can also be observed that the increase of the RE amount is accompanied by formation of lanthanide titanate ($Ln_2Ti_2O_7$, where Ln = $Eu^{3+}$, $Er^{3+}$) at progressively lower temperatures. The formation of the lanthanide titanate is probably favourable to the A–R phase transformation [42], catalyzing for high Ln content the mass transport to the nucleation region of the rutile phase, promoting rutile nuclei growth, and therefore the phase transformation. In the case of Eu- and Er-doped samples, the $Ln_2Ti_2O_7$ phase formation was observed at 900 °C and 1000 °C for 3 mol% and 1 mol% (Fig. 6), respectively, occurring at lower temperature for higher content.

In conclusion, the XRD results clearly indicated that rare earth ions had a strong inhibition effect on the anatase-to-rutile phase transition, but the inhibition effect was not proportional to the lanthanide concentration. In all cases, in general, 1 at.% lanthanide dopants exerted the strongest inhibition effect on the anatase-to-rutile phase transformation.

Cell parameters of the rutile phase are reported in Table 3, the reference for rutile being JCPDS #73-1765 ($a = b = 4.589(1)$ Å, $c = 2.954(3)$ Å, space group $P4_2/mnm(136)$, theoretical density 4.266 g/$cm^3$, $Z = 2$). As a general trend, a slight increment of the

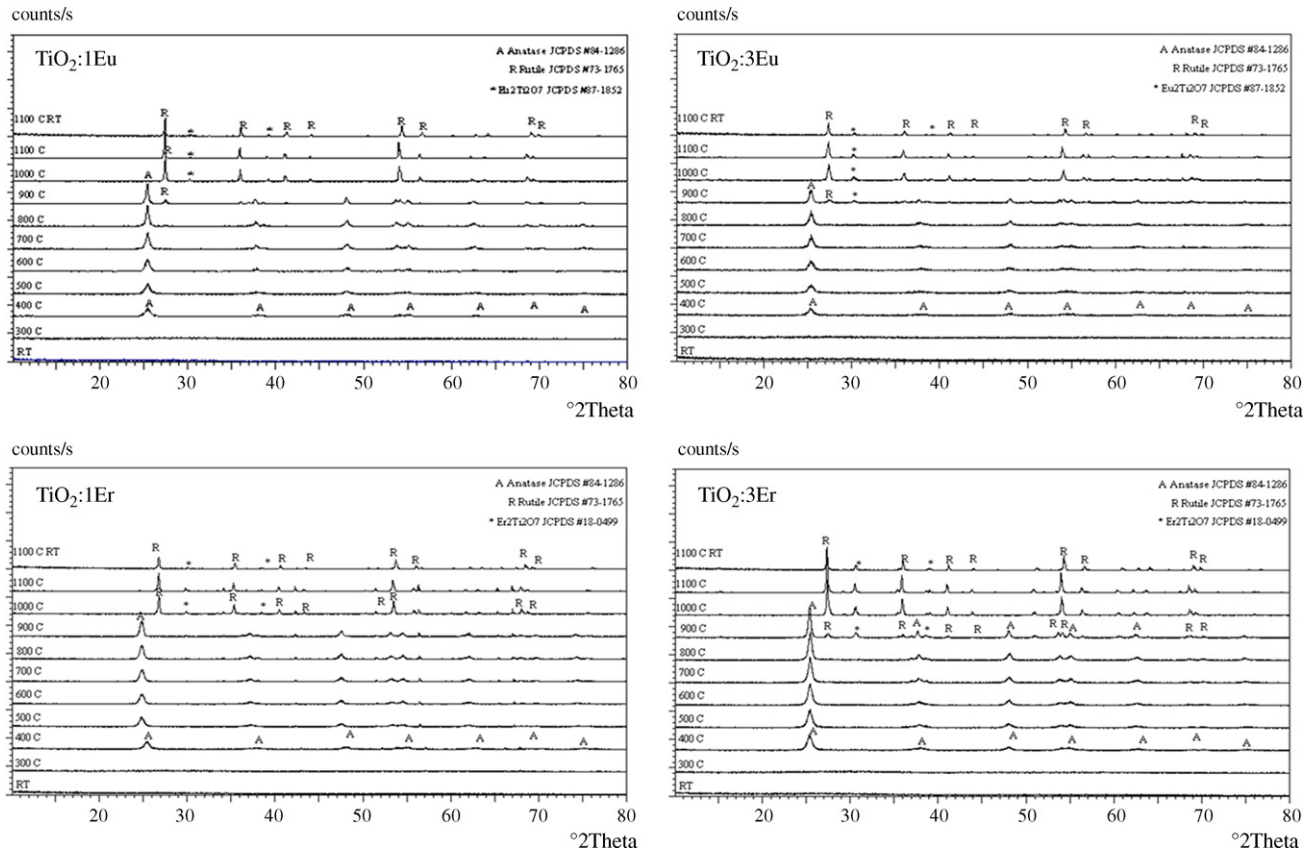


**Fig. 6.** HT-XRD patterns of $TiO_2$:1Eu, $TiO_2$:3Eu, $TiO_2$:1Er and $TiO_2$:3Er electrospun mats (pre-treated at 300 °C) from RT to 1100 °C.

reticular constants and of the unit cell volume was observed, due to the larger size of RE ionic radius compared to Ti one [42].

### 3.5. Raman spectroscopy characterisation of undoped and RE-doped ceramic nanofibers

As an important material structure research method, Raman spectrum technology has been used to further analyse and to identify the phase composition of all samples, allowing to distinguish the $TiO_2$ different structure types.

Raman spectra of *as spun* and calcined at 500 and 1000 °C samples are reported in Fig. 7a–c, respectively.

Particularly, in Fig. 7a comparison between the Raman spectra of *as spun* neat PVP, PVP/$TiO_2$ and PVP/$TiO_2$:3Er samples is reported, as an example. In the case of all *as spun* samples, the characteristic titania bands were not observed, indicating that the as prepared materials were indeed amorphous and free from any crystalline titania phases. All mats presented the typical Raman spectrum of PVP (Fig. 7a), characterised by peaks at 758 $cm^{-1}$ (C–N vibrations), at 899 $cm^{-1}$ ($CH_2$ *rocking* mode), at 935 $cm^{-1}$ (C–C *stretching*), at 1028 $cm^{-1}$ ($CH_2$ symmetric *stretching*), at 1232 $cm^{-1}$ (C–N *stretching*), at 1426 $cm^{-1}$ (C–H *bending*), at 1232 $cm^{-1}$ (C–N *stretching*), at 1426 $cm^{-1}$ (C–H *bending*), at 1663 $cm^{-1}$ (C=O vibration) and at 2928 $cm^{-1}$ (C–H *stretching*).

**Table 3**
Calculated cell parameters of undoped and RE-doped $TiO_2$ mats calcined at 1000 °C.

| Sample | *a* (Å) | *b* (Å) | *c* (Å) | *V* |
|---|---|---|---|---|
| $TiO_2$ | 4.585(2) | 4.585(2) | 2.959(1) | 62.213 |
| $TiO_2$:1La | 4.582(2) | 4.582(2) | 2.947(3) | 61.872 |
| $TiO_2$:1Eu | 4.5902(6) | 4.5902(6) | 2.95974(5) | 62.314 |
| $TiO_2$:3Eu | 4.5891(1) | 4.5891(1) | 2.9589(9) | 62.321 |
| $TiO_2$:1Er | 4.5874(9) | 4.5874(9) | 2.9563(7) | 62.213 |
| $TiO_2$:3Er | 4.587(1) | 4.587(1) | 2.9584(6) | 62.239 |

Raman spectra of undoped and RE-doped $TiO_2$ samples calcined at 500 °C showed similar patterns, characterised by the anatase typical peaks with Raman shifts at 146, 196, 396, 520 and 637 $cm^{-1}$ which correspond to the $E_g$, $E_g$, $B_{1g}$, $A_{1g}$ and $E_g$ vibration modes of anatase phase of $TiO_2$ ($A_{1g} + 2B_{1g} + 3E_g$), respectively [81] (Fig. 7b). It is worth underlining that the RE doping did not influence and change the structure of $TiO_2$, revealing both undoped and doped samples similar Raman peaks. This is consistent and in good agreement with the results obtained from the XRD analyses (Figs. 5 and 6).

The Raman analysis suggested that the dopant atoms with a relatively low level of doping (1–3 mol%) sited substitutionally on Ti sites in the anatase crystal structure, yielding the homogeneous distribution of the doped atoms in the anatase nanocrystalline structure.

These statements are supported by the XRD and EDS measurements, indicating the presence of the only anatase phase at 500 °C (Figs. 5 and 6) and the homogeneous distribution of the rare earth ions within the fibrous mats (Figs. 2 and 3), respectively.

After thermal treatment at 1000 °C (Fig. 7c) both undoped and doped nanofibers showed the rutile typical Raman active modes ($A_{1g} + B_{1g} + B_{2g} + E_g$).

The dominant lines at 444 and 609 $cm^{-1}$ are ascribed to the $E_g$ and $A_{1g}$ vibrational modes of rutile, respectively; the broad shoulder at about 828 $cm^{-1}$ is assigned to the $B_{2g}$ vibrational mode.

The Raman peak at 235 $cm^{-1}$ is known to be the compound vibration peak due to the multiple-Phonon scattering processes,

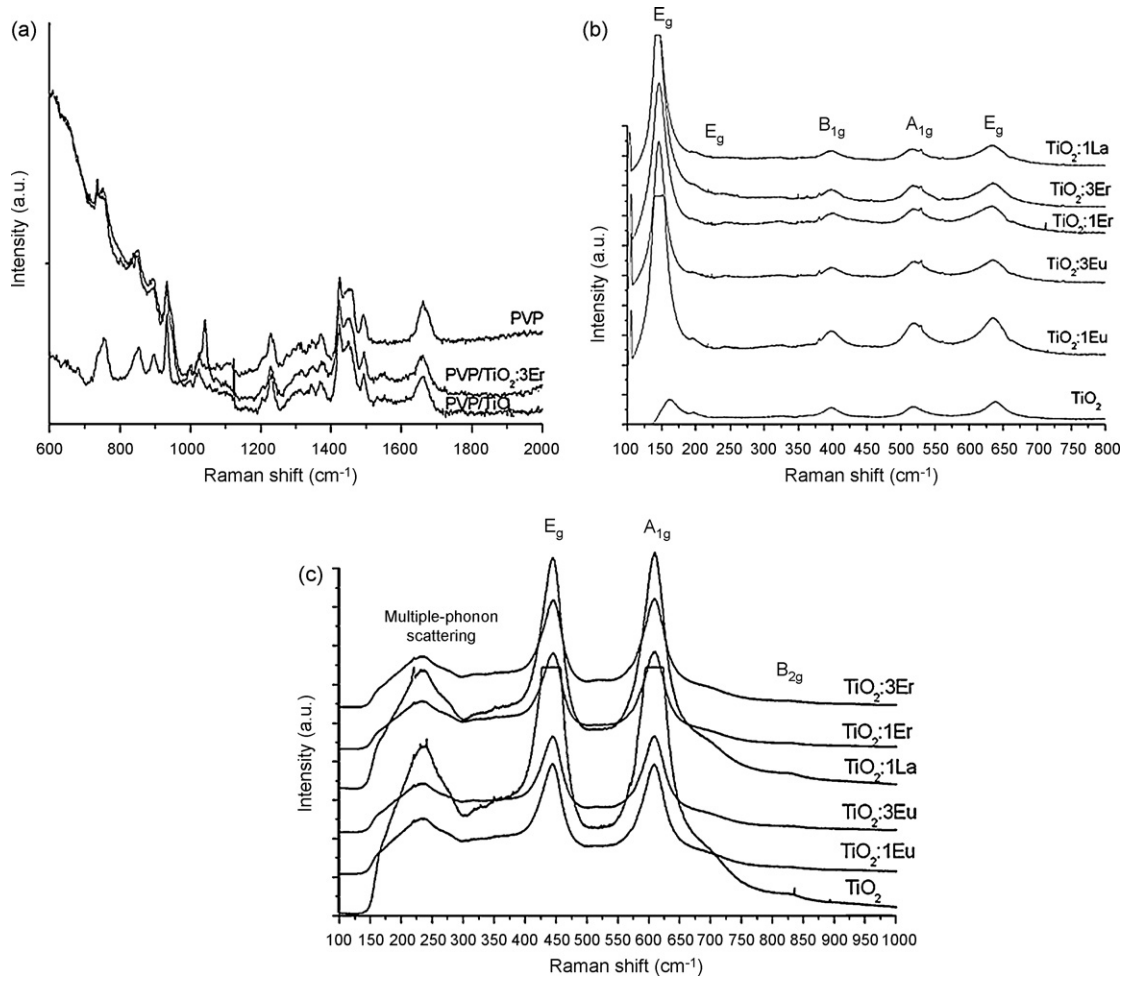


**Fig. 7.** Room temperature Raman spectra of *as spun* PVP, PVP/$TiO_2$ and PVP/$TiO_2$:3Er samples (a), Raman spectra of undoped and RE-doped $TiO_2$ nanofibers calcined at 500 °C (b) and calcined at 1000 °C (c).

which is also considered as a characteristic Raman peak of rutile type $TiO_2$ [82].

In conclusion, the Raman spectroscopy analysis confirmed the XRD phase evaluations, detecting the typical anatase phase vibrational modes at 500 °C and the rutile phase ones at 1000 °C.

### 3.6. Luminescence spectroscopy

In order to deeply investigate the luminescence properties, the room temperature emission spectra for the *as spun* and annealed at 500 and 1000 °C undoped and RE doped fibers were recorded either by means of Raman spectroscopy and by a scanning electron microscope FEG-SEM, equipped with a cathodoluminescence (CL) device.

PL and CL spectra can be also used in order to study the $TiO_2$ energy levels and to provide information about the surface oxygen vacancies and defects based on the electronic structure and optical characteristics [83,84] and about the differences between anatase and rutile phases. In fact, it has been reported that the structural dissimilarities between the anatase and the rutile phases govern the differences on their electrical and optical properties [85], acting, for the two phases, the defects as radiative and non-radiative centres. In Fig. 8a the CL spectra of *as spun* PVP mat and PVP/$TiO_2$ samples, before and after thermal treatment at 500 and 1000 °C, are reported. The CL spectrum of the *as spun* neat PVP mat shows a broad emission band centred at 650 nm, which might originate from the organic functional groups of PVP. In the case of PVP/$TiO_2$ mat, it is evident an overlapping of two broad emission bands due to the contribution of PVP (centred at about 650 nm) and $TiO_2$ precursor (centred around 550 nm). The PVP emission peak disappeared after calcination at 500 °C, due to polymer removal. In fact, after calcination at 500 °C, a broad green photoluminescence peak in the visible range peaking at about 550 nm was only detected in $TiO_2$ nanofibers and could be attributed to the radiative recombination of self-trapped excitons (STEs) localized within $TiO_6$ octahedra [86,87] and to the surface defects of $TiO_2$ nanofibers. The STE originates from band-to-band excitation where the excited electron and the remaining hole create a local deformation of $TiO_6$ octahedra and thus localize themselves into a state in the energy gap of $TiO_2$. In the basic $TiO_2$ cell, each $Ti^{4+}$ ion is surrounded by an octahedron of six $O^{2-}$ ions. Structural defects can be formed by losing a neutral oxygen atom during high temperature annealing, and the defect states associated with $Ti^{3+}$ ions appear to be introduced in the band-gap at 0.7–0.8 eV below $E_F$ [88,89].

Moreover, it is worth emphasizing the remarkable enhancement of the cathodoluminescence intensity of $TiO_2$ nanofibers, after thermal treatment at 500 °C, with respect to both the *as spun* neat PVP and the PVP/$TiO_2$ mats.

In fact, the intensity of the UV emission is strongly influenced by the material crystallinity (and thus by the correspondent decrease of impurity and structural defects, i.e. oxygen vacancy, dislocations) and by the diameter of the obtained nanofibers. Therefore, the green emission band intensity enhancement, observed for the

calcined at 500 °C $TiO_2$ nanofibers, can be easily correlated to their high surface-to-volume ratio which promotes the existence of either large quantities of oxygen vacancies or defects. In general, with decrease in the particle size the oxygen vacancy number enhances and the probability of exciton occurrence increases, resulting the luminescence signal stronger [88].

The CL spectrum of the undoped $TiO_2$ nanofibers after calcination at 1000 °C in air presented a remarkably intense emission

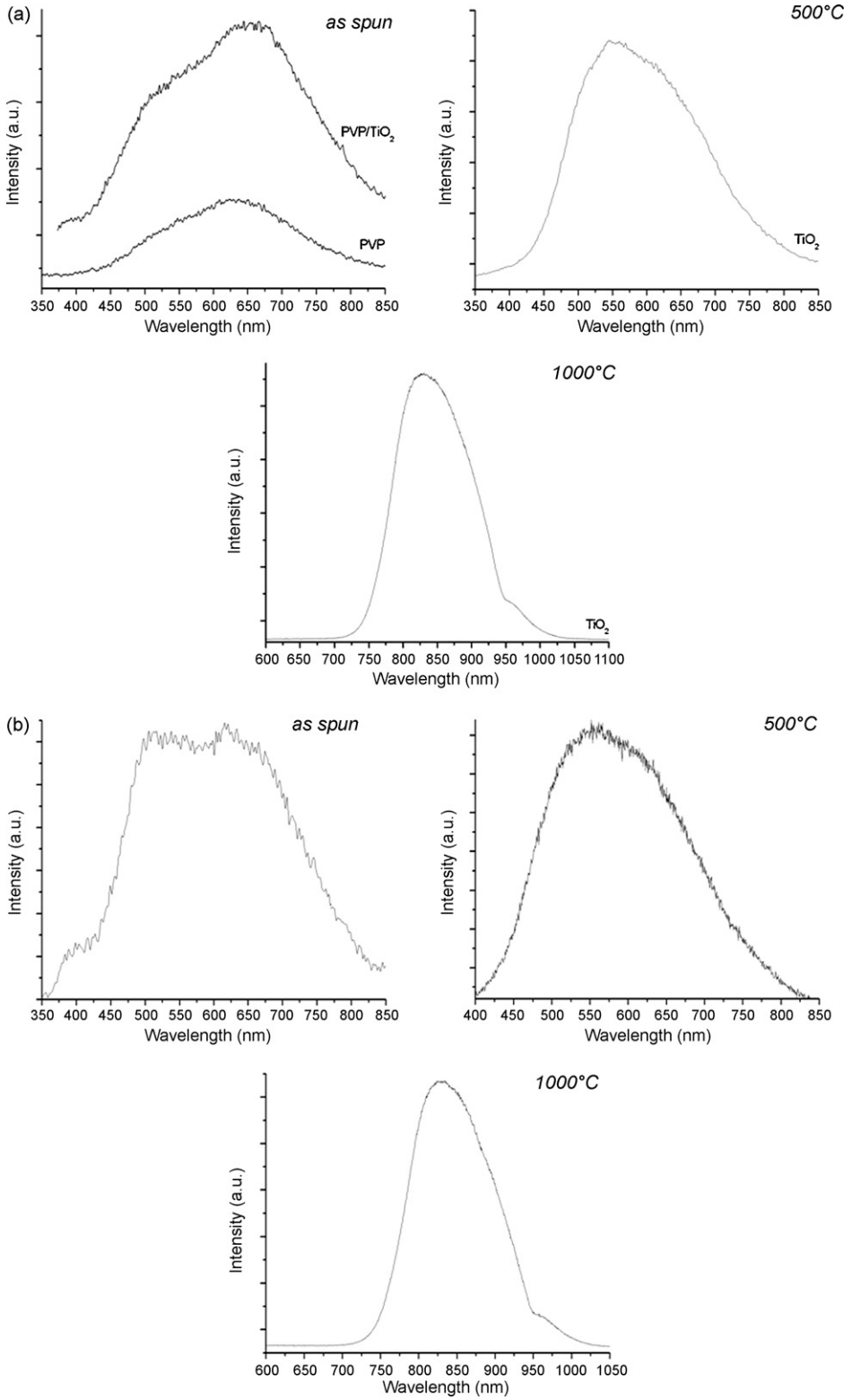


**Fig. 8.** (a) Cathodoluminescence (CL) spectra of neat PVP, PVP/$TiO_2$ precursor electrospun mat and $TiO_2$ electrospun mat calcined at 500 °C and at 1000 °C. (b) Cathodoluminescence (CL) spectra of PVP/$TiO_2$:1La, $TiO_2$:1La calcined at 500 °C and $TiO_2$:1La calcined at 1000 °C. (c) Cathodoluminescence (CL) spectra of PVP/$TiO_2$:3Eu, $TiO_2$:3Eu calcined at 500 °C and $TiO_2$:3Eu calcined at 1000 °C. (d) Photoluminescence (PL) spectra of PVP/$TiO_2$:3Eu, $TiO_2$:3Eu calcined at 500 °C and $TiO_2$:3Eu calcined at 1000 °C. (e) Cathodoluminescence (CL) spectra of PVP/$TiO_2$:3Er, $TiO_2$:3Er calcined at 500 °C and $TiO_2$:3Er calcined at 1000 °C.

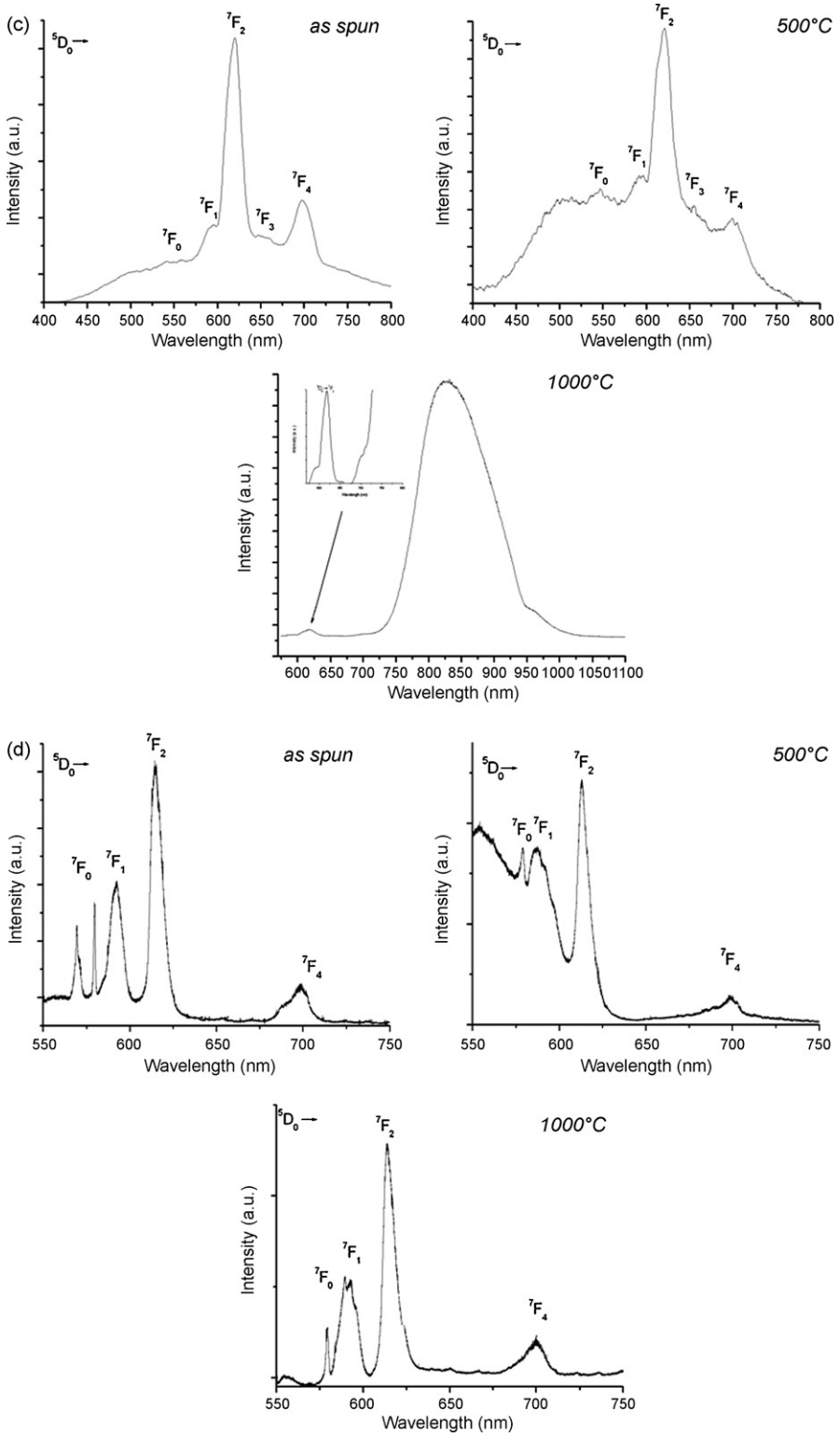


**Fig. 8.** (*Continued*)

peak in infrared region situated at about 835 nm. This peak is ascribable to the photoluminescence transitions associated to the $Ti^{3+}$ interstitial ions in rutile single crystal and to the continuous losing of oxygen atoms with the increase of annealing temperature [90], in good agreement with the XRD and Raman considerations.

The luminescence spectra of Eu-, La-, Er-doped samples, before and after thermal treatment, are reportedin Fig. 8b–d, and they clearly testify the presence of the lanthanide ions in the $TiO_2$ host, in the case of Eu- and Er-doped samples.

For La-doped sample, we obtained similar CL spectra compared to undoped $TiO_2$ ones (Fig. 8b). This indicates that $La^{3+}$ doping does not cause a new luminescent phenomenon, but affects the response range and intensity of CL spectra [88].

On the other side, Eu- and Er-doped samples showed a strong laser induced luminescence in the visible region, due to the tran-

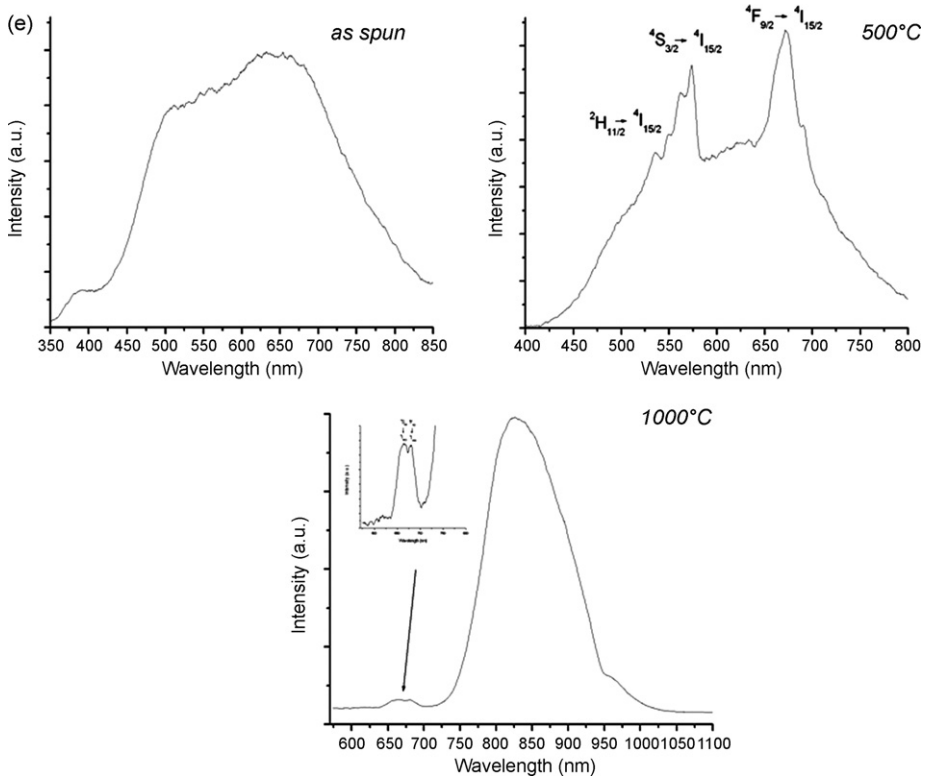


**Fig. 8.** (*Continued*)

sitions of the correspondent RE ion. In agreement with previous literature results [91,92], the luminescence spectra of all samples were characterised by inhomogeneously broadened bands, typical of $Eu^{3+}$ and $Er^{3+}$ doped disordered systems.

Particularly, the obtained CL spectra for 3 mol% Eu doped sample are shown in Fig. 8c, as an example. Characteristic emissions due to $Eu^{3+}$ 4f–4f transitions from the $^5D_0$ excited level to $^7F_J$ manifolds of the $4f^6$ configuration were detected in the spectra of both *as spun* and calcined at 500 °C samples. Besides a strong emission attributed to the $^5D_0 \rightarrow {}^7F_2$ transition of $Eu^{3+}$ (around 615 nm), additional bands attributed to the transitions $^5D_0 \rightarrow {}^7F_0$ (around 580 nm), $^5D_0 \rightarrow {}^7F_1$ (around 595 nm), $^5D_0 \rightarrow {}^7F_3$ (around 652 nm) and $^5D_0 \rightarrow {}^7F_4$ (around 700 nm) were observed. The red colour of the strong luminescence signal is seen by the naked eye, due to the $^5D_0 \rightarrow {}^7F_2$ transition. It is important to note that the contribution of the titania broad band at 550 nm, due to recombination of STE, was detected in the CL spectrum of mat thermally treated at 500 °C (Fig. 8c). After the calcination at 1000 °C, in the CL pattern, it was possible to individuate only the main peak at about 615 nm and it was evident that the intensity of this red emission peak decreased and the near-infrared emission peaking at about 835 nm appeared. This peak could be associated to the rutile phase.

In all cases, the emission bands were broad with respect to those commonly observed for many $Eu^{3+}$ doped crystalline hosts, such as sesquioxides (i.e. $Y_2O_3$, $Lu_2O_3$) [93] and garnets (i.e. $Y_3Al_5O_{12}$, $Gd_3Ga_5O_{12}$) [94]. Moreover, the transitions between the $^5D_0$ and the $^7F_J$ Stark levels were not clearly resolved. This behaviour pointed to a relevant disorder of the $Eu^{3+}$ ions in the $TiO_2$ host environment. The asymmetry of the $Eu^{3+}$ ion coordination polyhedron can be estimated by the asymmetry ratio ($R$), defined as

$$R = \frac{I(^5D_0 \rightarrow {}^7F_2)}{I(^5D_0 \rightarrow {}^7F_1)}$$

where $I(^5D_0 \rightarrow {}^7F_2)$ is the intensity of the $^5D_0 \rightarrow {}^7F_2$ transition and $I(^5D_0 \rightarrow {}^7F_1)$ of the $^5D_0 \rightarrow {}^7F_1$ one [95]. In particular, the lower the $R$ value is, the higher is the site symmetry at the $Eu^{3+}$ ion.

Thus, in order to estimate the asymmetry ratio values for Eu-doped samples, we used the PL spectra. In fact, all the PL patterns of the mats calcined at 500 °C and 1000 °C presented defined transitions peaks. In particular, the 550 nm PL signal due to recombination of STE disappeared after annealing at 500 °C, mainly due to the resonant energy transfer from STE to $Eu^{3+}$ ions and, after the calcination at 1000 °C, the PL spectra clearly showed the characteristic $Eu^{3+}$ emissions (Fig. 8d).

The value of the asymmetry parameter for the $Eu^{3+}$ doped nanofibers resulted to be $1.3 \pm 0.1$ and $2.0 \pm 0.1$ for the PVP/$TiO_2$ samples doped with 1% and 3% of $Eu^{3+}$, respectively (Table 4). These values were lower than that reported (6.6) for the bare Eu complex [96], indicating that the $Eu^{3+}$ ions in the PVP/$TiO_2$ samples were accommodated in a site with higher symmetry with respect to the bare europium complex. The $R$ values for the $TiO_2$ nanofibers calcined at 500 °C were $4.2 \pm 0.1$ and $4.14 \pm 0.1$ for the 1% and 3% Eu-doped samples, respectively (Table 4).

After the annealing at 1000 °C, the $R$ values of the samples $TiO_2$:1Eu and $TiO_2$:3Eu were $2.1 \pm 0.1$ and $2.2 \pm 0.1$, respectively. The $R$ values for both Eu doping content of $TiO_2$ nanofibers resulted lower than those found for $Eu^{3+}$ doped nanocrystalline $TiO_2$ powders prepared by a radio frequency thermal plasma oxidation technique ($R = 9.7$) [97] and by a sol–gel technique ($R = 6.2$) [98]

**Table 4**
Estimated asymmetry ratio ($R$) values of Eu-doped nanofibers before and after thermal treatments at 500 °C and 1000 °C.

| Sample | $R$_as spun | $R$_500 °C | $R$_1000 °C |
|---|---|---|---|
| $TiO_2$:1Eu | 1.3 ± 0.1 | 4.2 ± 0.1 | 2.1 ± 0.1 |
| $TiO_2$:3Eu | 2.0 ± 0.1 | 4.1 ± 0.1 | 2.2 ± 0.1 |

(Table 4). In any case, these *R* values did not agree with the relatively high symmetry of the $Ti^{4+}$ ions in the anatase structure ($D_{2d}$), as this symmetry was not compatible with a hypersensitive behaviour of the $^5D_0 \rightarrow {}^7F_2$ transition [99].

In the case of *as spun* Er-doped samples, the CL spectra were dominated by the overlapping of the $TiO_2$ precursor broad emission peaking at about 550 nm and the PVP broad band centred at 650 nm with no emission of $Er^{3+}$ ions, as showed in Fig. 8e for sample PVP/$TiO_2$:3Er, in good agreement with Jia et al. [67]. After the annealing at 500 °C, green CL peaking at 566.6 nm due to the intra-4f transition of $^4S_{3/2} \rightarrow {}^4I_{15/2}$ of $Er^{3+}$ ions in the $TiO_2$ matrix was detected. Moreover, other weaker emissions at 528.1 and 669.3 nm were identified and could be assigned to intra-4f transitions of $^2H_{11/2} \rightarrow {}^4I_{15/2}$ and $^4F_{9/2} \rightarrow {}^4I_{15/2}$ of $Er^{3+}$ ions, respectively. Extra weaker emission peaks could be ascribed to distinct optical transitions of the $Er^{3+}$ ions. It is worth underlining that the contribution of the broad band at 550 nm was evident. With the increase of annealing temperature up to 1000 °C, in the CL spectra low intensity overlapped emission bands at about 665 and 680 $cm^{-1}$ were relieved and a very intense band centred at about 835 nm due to the rutile phase was observed.

Summarizing, for all RE-doped $TiO_2$ samples, after calcination at 1000 °C, in the CL spectra, the intensity of characteristic emission peaks decreased and the near-infrared emission peaking at about 835 nm, due to the rutile phase, appeared.

For the anatase nanofibers, the electrons are excited to the conduction band of $TiO_2$ nanofibers by absorbing the photon energy and this energy is directly transferred to RE ions from $TiO_2$ nanofibers. For rutile $TiO_2$ nanofibers, the energy of 1.53 eV associated with $Ti^{3+}$ interstitial ions is lower than the transition energy of RE ions. Thus, the energy was back transferred from RE dopant to defect level associated with $Ti^{3+}$ interstitial ions. Furthermore 835 nm emission of $TiO_2$:RE is stronger than that of undoped $TiO_2$ nanofibers, as also reported in other Refs. [70,71]. So we can conclude the energy back transfer is responsible for the luminescence at 835 nm.

Moreover, as mentioned previously, the radii of the rare-earth ions are too large to allow them to replace $Ti^{4+}$ in an anatase crystal, and the unresolved luminescence spectra are consistent with rare earths in a glass-like environment. These evidences suggest that the rare-earth ions could be located at the edge of the $TiO_2$ nanocrystallites, or in close proximity to the surface states of $TiO_2$ crystals. However, in the light of previously discussed XRD and Raman results, we can hypothesize the substitution of Ln ions at Ti sites. On the basis of these overall findings, we can thus conclude that some Ln dopant ions are sited substitutionally at the Ti sites and other ones located at the edge of $TiO_2$ nanocrystallites.

Because of the small size and the large number of nanocrystallites in these materials, a great number of the surface states are available to transfer the energy to the crystal field states of the rare-earth ions.

In conclusion, a possible energy transfer process might consist in the following: the band gap of titania absorbes UV light, then relaxes it to the surface states, followed by the energy transfer to the crystal field states of the rare-earth ions.

## 4. Conclusions

The combination of sol–gel process and electrospinning technique allows the fabrication of organic–inorganic fibers. The hybrid electrospun fibers originate ceramic nanofibers after a suitable thermal treatment in order to eliminate the organic component. Undoped and RE (RE = Eu, Er, La)-doped $TiO_2$ nanofibers were successfully produced by electrospinning, using a $Ln^{3+}$ concentration ranging between 1 and 3 mol%. The average fiber size was about 40 nm for neat $TiO_2$ fibers and ranged between $40 \pm 10$ nm and $77 \pm 19$ nm for the RE-doped. The XRD analysis confirmed that the rare earth doping delayed the anatase-to-rutile phase transition, the effect depending on the amount of doping. In the case of Eu- and Er-doped nanofibers, the formation of lanthanide–titanium oxide ($Ln_2Ti_2O_7$) occurred in the temperature range 900–1000 °C, depending on the $Ln^{3+}$ content. The La-doped nanofibers presented similar luminescence spectra compared to undoped $TiO_2$ ones. This indicated that $La^{3+}$ doping did not cause a new luminescent phenomenon, but affected the response range and intensity of PL spectra. The Eu- and Er-doped samples, before and after thermal treatment, showed a strong luminescence emission due to the transitions of the correspondent $Ln^{3+}$ ions. The relevant broadening of the emission bands pointed to a notable disorder environment around the lanthanide ions in the titania host, typical of $Eu^{3+}$ and $Er^{3+}$ doped systems.

## Acknowledgements

The authors wish to acknowledge Dr. Alessandro Alan Porporati for his support in luminescence measurements.

## References

[1] S. Rodrigues, K.T. Ranjit, S. Uma, I.N. Martyanov, K.J. Klabunde, Single-step synthesis of a highly active visible-light photocatalyst for oxidation of a common indoor air pollutant: acetaldehyde, Adv. Mater. 17 (20) (2005) 2467–2471.
[2] H. Kisch, W. Macyk, Visible-light photocatalysis by modified titania, Chem. Phys. Chem. 3 (2002) 399–400.
[3] A.P. Davis, D.L. Green, Green photocatalytic oxidation of cadmium–EDTA with titanium dioxide, Environ. Sci. Technol. 33 (4) (1999) 609–617.
[4] H. Choi, A.C. Sofranko, D.D. Dionysiou, Nanocrystalline $TiO_2$ photocatalytic membranes with a hierarchical mesoporous multilayer structure: synthesis, characterization, and multifunction, Adv. Funct. Mater. 16 (8) (2006) 1067–1074.
[5] Z.M. El-Bahy, A.A. Ismaila, R.M. Mohamed, Enhancement of titania by doping rare earth for photodegradation of organic dye (Direct Blue), J. Hazard. Mater. 166 (1) (2009) 138–143.
[6] A. Fujishima, K. Hashimoto, T. Watanabe, $TiO_2$ Photocatalysis Fundamentals and Applications, BKC Inc., Tokyo, 1999.
[7] H. Hayashi, K. Torii, Hydrothermal synthesis of titania photocatalyst under subcritical and supercritical water conditions, J. Mater. Chem. 12 (2002) 3671–3676.
[8] A.P. Hong, D.W. Bahnemann, M.R. Hoffmann, Cobalt(II) tetrasuifophthalocyanine on titanium dioxide: a new efficient electron relay for the photocatalytic formation and depletion of hydrogen peroxide in aqueous suspensions, J. Phys. Chem. 91 (8) (1987) 2109–2117.
[9] M.R. Hoffmann, S.T. Martin, W.Y. Choi, D.W. Bahnemann, Environmental applications of semiconductor photocatalysis, Chem. Rev. 95 (1995) 69–96.
[10] B. O'Regan, M. Grãtzel, A low-cost, high-efficiency solar cell based on dye-sensitized colloidal $TiO_2$ films, Nature 353 (1991) 737–740.
[11] M.A. Fox, M.Y. Dulay, Heterogeneous photocatalysis, Chem. Rev. 93 (1) (1993) 341–357.
[12] G. Sivalingam, K. Nagaveni, M.S. Hegde, G. Madras, Photocatalytic degradation of various dyes by combustion synthesized nano anatase $TiO_2$, Appl. Catal. B: Environ. 45 (1) (2003) 23–38.
[13] P. Mohapatra, K.M. Parida, Photocatalytic activity of sulfate modified titania 3: decolorization of methylene blue in aqueous solution, J. Mol. Catal. A: Chem. 258 (2006) 118–123.
[14] I. Hayakawa, Y. Iwamoto, K. Kikuta, S. Hirano, Gas sensing properties of platinum dispersed-$TiO_2$ thin film derived from precursor, Sens. Actuators B 62 (1) (2000) 55–60.
[15] A. Bahtat, M. Bouazaoui, M. Bahatat, C. Garapon, B. Jacquier, J. Mugnier, Up-conversion fluorescence spectroscopy in $Er^{3+}$:$TiO_2$ planar waveguides prepared by a sol–gel process, J. Non-Cryst. Solids 202 (1996) 16–22.
[16] U. Bach, D. Lupo, P. Comte, J.E. Moser, F. Weissortel, J. Salbeck, H. Spreitzer, M. Gratzel, Solid-state dye-sensitized mesoporous $TiO_2$ solar cells with high photon-to-electron conversion efficiencies, Nature 395 (1998) 583–585.
[17] C.A. Linkous, G.J. Carter, D.B. Locuson, A.J. Ouellette, D.K. Slattery, L.A. Smitha, Photocatalytic inhibition of algae growth using $TiO_2$, $WO_3$, and cocatalyst modifications, Environ. Sci. Technol. 34 (22) (2000) 4754–4758.
[18] H. Hidaka, Y. Asai, J. Zhao, K. Nohara, E. Pelizzetti, N. Serpone, Photoelectrochemical decomposition of surfactants on a $TiO_2$ particulate film electrode assembly, J. Phys. Chem. 99 (20) (1995) 8244–8248.
[19] S. Rajeshkumar, C. Suresh, A.K. Vasudevan, N.R. Suja, P. Mukundan, K.G.K. Warrier, Phase transformation in sol–gel titania containing silica, Mater. Lett. 38 (3) (1999) 161–166.

[20] D. Vorkapic, T. Matscukas, Effect of temperature and alcohols in the preparation of titania nanoparticles from alkoxides, J. Am. Ceram. Soc. 81 (11) (1998) 2815–2820.

[21] H. Zhang, J.F. Banfield, Phase transformation of nanocrystalline anatase-to-rutile via combined interface and surface nucleation, J. Mater. Res. 15 (2) (2000) 437–448.

[22] J.S. Song, D.Y. Lee, W.J. Lee, S.J. Kim, Redox abilities of rutile $TiO_2$ ultrafine powder in aqueous solutions, Met. Mater. Int. 8 (1) (2002) 103–109.

[23] J. Arbiol, J. Cerdà, G. Dezanneau, A. Cirera, F. Peiró, A. Cornet, J.R. Morante, Effects of Nb doping on the $TiO_2$ anatase-to-rutile phase transition, J. Appl. Phys. 92 (2) (2002) 853–861.

[24] S. Karvinen, The effects of trace elements on the crystal properties of $TiO_2$, Solid State Sci. 5 (2003) 811–819.

[25] Y.H. Zhang, A. Reller, Nanocrystalline iron-doped mesoporous titania and its phase transition, J. Mater. Chem. 11 (2001) 2537–2541.

[26] Y.H. Zhang, A. Reller, Phase transformation and grain growth of doped nanosized titania, Mater. Sci. Eng. C 19 (2002) 323–326.

[27] Y.H. Zhang, A. Weidenkaff, A. Reller, Mesoporous structure and phase transition of nanocrystalline $TiO_2$, Mater. Lett. 54 (2002) 375–381.

[28] C.P. Sibu, S. Rajesh Kumar, P. Mukundan, K.G.K. Warrier, Structural modifications, associated properties of lanthanum oxide doped sol–gel nanosized titanium oxide, Chem. Mater. 14 (7) (2002) 2876–2881.

[29] R.J. Berry, M.R. Mueller, Photocatalytic decomposition of crude oil slicks using $TiO_2$ on a floating substrate, Microchem. J. 50 (1994) 28–32.

[30] J. Augustynski, The role of the surface intermediates in the photoelectrochemical behaviour of anatase and rutile $TiO_2$, Electrochim. Acta 38 (1) (1993) 43–46.

[31] M. Grätzel, Perspectives for dye-sensitized nanocrystalline solar cells, Prog. Photovolt. Res. Appl. 8 (1) (2000) 171–185.

[32] J.A. Navo, J.J. Testa, P. Djedjeian, J.R. Padron, D. Rodryguez, M.I. Litter, Iron-doped titania powders prepared by a sol–gel method—Part II: photocatalytic properties, Appl. Catal. A: Gen. 178 (2) (1999) 191–203.

[33] K.E. Karakitsou, X.E. Verykios, Effects of altervalent cation doping of titania on its performance as a photocatalyst for water cleavage, J. Phys. Chem. 97 (6) (1993) 1184–1189.

[34] S.T. Martin, C.L. Morrison, M.R. Hoffmann, Photochemical mechanism of size-quantized vanadium-doped $TiO_2$, J. Phys. Chem. 98 (1994) 13695–13704.

[35] H. Schneider, A. Baiker, V. Schar, A. Waukaun, Chromia on titania-IV. Nature of active sites for selective catalytic reduction of NO by $NH_3$, J. Catal. 146 (2) (1994) 545–556.

[36] J. Yang, J.M.F. Ferreira, Inhibitory effect of the $Al_2O_3$–$SiO_2$ mixed additives on the anatase–rutile phase transformation, Mater. Lett. 36 (1998) 320–324.

[37] M. Zalas, M. Laniecki, Photocatalytic hydrogen generation over lanthanides-doped titania, Sol. Energy Mater. Sol. Cells 89 (2005) 287–296.

[38] Y. Xie, C. Yuan, X. Li, Photocatalytic degradation of X-3B dye by visible light using lanthanide ion modified titanium dioxide hydrosol system, Colloids Surf. A: Physicochem. Eng. Aspects 252 (2005) 87–94.

[39] X. Yan, J. He, D. Evans, X. Duan, Y. Zhu, Preparation, characterization and photocatalytic activity of Si-doped and rare earth-doped $TiO_2$ from mesoporous precursors, Appl. Catal. B: Environ. 55 (2005) 243–252.

[40] H. Cuiying, Y. Wansheng, D. Liqin, L. Zhibin, S. Zhengang, Z. Lancui, Effect of $Nd^{3+}$ doping on photocatalytic activity of $TiO_2$ nanoparticles for water decomposition to hydrogen, Chin. J. Catal. 27 (3) (2006) 203–209.

[41] T. Peng, D. Zhao, H. Song, C. Yan, Preparation of lanthana-doped titania nanoparticles with anatase mesoporous walls and high photocatalytic activity, J. Mol. Catal. A: Chem. 238 (2005) 119–126.

[42] Y. Zhang, H. Zhang, Y. Xu, Y. Wang, Significant effect of lanthanide doping on the texture and properties of nanocrystalline mesoporous $TiO_2$, J. Solid State Chem. 177 (2004) 3490–3498.

[43] F.B. Li, X.Z. Li, M.F. Hou, Photocatalytic degradation of 2-mercaptobenzothiazole in aqueous $La^{3+}$–$TiO_2$ suspension for odor control, Appl. Catal. B: Environ. 48 (3) (2004) 185–194.

[44] P. Mohapatra, S.K. Samantaray, K.M. Parida, Photocatalytic reduction of hexavalent chromium in aqueous solution over sulphate modified titania, J. Photochem. Photobiol. A: Chem. 170 (2005) 189–194.

[45] Y.H. Zhang, S.G. Ebbinghaus, A. Weidenkaff, T. Kurz, H.-A.K. von Nidda, P.J. Klar, M. Güngerich, A. Reller, Controlled iron-doping of macrotextured nanocrystalline titania, Chem. Mater. 15 (21) (2003) 4028–4033.

[46] W. Choi, A. Termin, M.R. Hoffmann, The role of metal ion dopants in quantum-sized $TiO_2$: correlation between photoreactivity and charge carrier recombination dynamics, J. Phys. Chem. 98 (51) (1994) 13669–13679.

[47] B. Ohtani, R.M. Bowman, D.P. Colombo, H. Kominami, H. Noguchi, K. Uosaki, Femtosecond diffuse reflectance spectroscopy of aqueous titanium(IV) oxide suspension: correlation of electron-hole recombination kinetics with photocatalytic activity, Chem. Lett. 27 (7) (1998) 579.

[48] R. Gopalan, Y.S. Lin, Evolution of pore and phase structure of sol-gel derived lanthana doped titania at high temperatures, Ind. Eng. Chem. Res. 34 (1995) 1189–1195.

[49] G. Boschloo, A. Hagfeldt, Photoinduced absorption spectroscopy of dye-sensitized nanostructured $TiO_2$, Chem. Phys. Lett. 370 (2003) 381–386.

[50] M.S.P. Francisco, V.R. Mastelaro, Inhibition of the anatase–rutile phase transformation with addition of $CeO_2$ to CuO–$TiO_2$ system: Raman spectroscopy, X-ray diffraction, and textural studies, Chem. Mater. 14 (6) (2002) 2514–2518.

[51] J.P. Shoffner, Use of tris-(6,6,7,7,8,8,8-heptafluoro-2,2-dimethyl-3,5-octanedionato)europium(III) for the structure determination and quantitative analysis of phenols, Anal. Chem. 47 (2) (1975) 341–343.

[52] D.L. Rabenstein, Applications of paramagnetic shift reagents in proton magnetic resonance spectrometry. Analysis of alcohol mixtures, Anal. Chem. 43 (12) (1971) 1599–1605.

[53] K.T. Ranjit, I. Willner, S.H. Bossmann, A.M. Braun, Lanthanide oxide-doped titanium dioxide photocatalysts: novel photocatalysts for the enhanced degradation of *p*-chlorophenoxyacetic acid, Environ. Sci. Technol. 35 (7) (2001) 1544–1549.

[54] J. Lin, J.C. Yu, An investigation on photocatalytic activities of mixed $TiO_2$-rare earth oxides for the oxidation of acetone in air, J. Photochem. Photobiol. A: Chem. 116 (1998) 63–67.

[55] D.W. Hwang, J.S. Lee, W. Li, S.H. Oh, Electronic band structure and photocatalytic activity of $Ln_2Ti_2O_7$ (Ln = La, Pr, Nd), J. Phys. Chem. B 107 (21) (2003) 4963–4970.

[56] C.V. Rice, D. Raftery, Photocatalytic oxidation of trichloroethylene using $TiO_2$ coated optical microfibers, Chem. Commun. 10 (1999) 895–896.

[57] S. Horikoshi, N. Watanabe, H. Onishi, H. Hidaka, N. Serpone, Photodecomposition of a nonylphenol polyethoxylate surfactant in a cylindrical photoreactor with $TiO_2$ immobilized fiberglass cloth, Appl. Catal. B: Environ. 37 (2) (2002) 117–129.

[58] T. Reztsova, C.-H. Chang, J. Koresh, H. Idriss, Dark- and photoreactions of ethanol and acetaldehyde over $TiO_2$/carbon molecular sieve fibers, J. Catal. 185 (1) (1999) 223–235.

[59] G. Goutailler, C. Guillard, S. Daniele, L.G. Hubert-Pfalzgraf, Low temperature and aqueous sol–gel deposit of photocatalytic active nanoparticulate $TiO_2$, J. Mater. Chem. 13 (2003) 342–346.

[60] D. Li, Y. Xia, Fabrication of titania nanofibers by electrospinning, Nano Lett. 3 (2003) 555–560.

[61] A. Kumar, R. Jose, K. Fujihara, J. Wang, S. Ramakrishna, Structural and optical properties of electrospun $TiO_2$ nanofibers, Chem. Mater. 19 (2007) 6536–6542.

[62] W.E. Teo, S. Ramakrishna, A review on electrospinning design and nanofibre assemblies, Nanotechnology 17 (14) (2006) R89–R106.

[63] T.B. Bini, S. Gao, T.C. Tan, S. Wang, A. Lim, L.B. Hai, S. Ramakrishna, Electrospun poly(L-lactide-co-glycolide) biodegradable polymer nanofibre tubes for peripheral nerve regeneration, Nanotechnology 15 (2004) 1459–1464.

[64] H. Zhang, H. Song, B. Dong, L. Han, G. Pan, X. Bai, L. Fan, S. Lu, H. Zhao, F. Wang, Electrospinning preparation and luminescence properties of europium complex/polymer composite fibers, J. Phys. Chem. C 112 (2008) 9155–9162.

[65] W. Sigmund, J. Yuh, H. Park, V. Maneeratana, G. Pyrgiotakis, A. Daga, J. Taylor, J.C. Nino, Processing and structure relationships in electrospinning of ceramic fiber systems, J. Am. Ceram. Soc. 89 (2) (2006) 395–407.

[66] Y.Z. Zhang, J. Venugopal, Z.-M. Huang, C.T. Lim, S. Ramakrishna, Crosslinking of the electrospun gelatine nanofibers, Polymer 47 (8) (2006) 2911–2917.

[67] C.W. Jia, J.G. Zhao, H.G. Duan, E.Q. Xie, Visible photoluminescence from $Er^{3+}$-doped $TiO_2$ nanofibres by electrospinning, Mater. Lett. 61 (22) (2007) 4389–4392.

[68] V. Tomer, R. Teye-Mensah, J.C. Tokash, N. Stojilovic, W. Kataphinan, E.A. Evans, G.G. Chase, R.D. Ramsier, D.J. Smith, D.H. Reneker, Selective emitters for thermophotovoltaics: erbia-modified electrospun titania nanofibers, Sol. Energy Mater. Sol. Cells 85 (2005) 477–488.

[69] E.T. Bender, R. Wang, M.T. Aljarrah, E.A. Evans, R.D. Ramsier, Synthesis and characterization of erbia doped metal oxide nanofibers for applications in thermophotovoltaics, J. Vac. Sci. Technol. A: Vac. Surf. Films) 25 (4) (2007) 922–926.

[70] J. Zhao, C. Jia, H. Duan, Z. Sun, X. Wang, E. Xie, Structural and photoluminescence properties of europium-doped titania nanofibers prepared by electrospinning method, J. Alloys Compd. 455 (2008) 497–500.

[71] J. Zhao, H. Duan, Z. Ma, L. Liu, E. Xie, Effect of temperature on the photoluminescence of $Eu^{3+}$ doped $TiO_2$ nanofibers prepared by electrospinning, J. Optoelectron. Adv. Mater. 10 (10) (2008) 3029–3032.

[72] H. Wang, Y. Wang, Y. Yang, X. Li, C. Wang, Photoluminescence properties of the rare-earth ions in the $TiO_2$ host nanofibers prepared via electrospinning, Mater. Res. Bull. 44 (2009) 408–414.

[73] D. Xu, L. Feng, A. Lei, Characterizations of lanthanum trivalent ions/$TiO_2$ nanopowders catalysis prepared by plasma spray, J. Colloid Interface Sci. 329 (2009) 395–403.

[74] S. Ramakrishna, K. Fujihara, W.E. Teo, T.C. Lim, Z. Ma, An Introduction to Electrospinning and Nanofibers, World Scientific, Singapore, 2005.

[75] S.A. Theron, E. Zussman, A.L. Yarin, Experimental investigation of the governing parameters in the electrospinning of polymer solutions, Polymer 45 (6) (2004) 2017–2030.

[76] A. Bianco, I. Cacciotti, M.E. Fragalà, F.R. Lamastra, A. Speghini, F. Piccinelli, G. Malandrino, G. Gusmano, Eu-doped titania nanofibers: processing, thermal behaviour and luminescent properties, J. Nanosci. Nanotechnol. 10 (2010) 5183–5190.

[77] S.V. Fridrikh, J.H. Yu, M.P. Brenner, G.C. Rutledge, Controlling the fiber diameter during electrospinning, Phys. Rev. Lett. 90 (14) (2003), 144502(1)–144502(4).

[78] J. Watthanaarun, P. Supaphol, V. Pavarajarn, Photocatalytic activity of neat and silicon-doped titanium(IV) oxide nanofibers prepared by combined sol-gel and electrospinning techniques, J. Nanosci. Nanotechnol. 7 (7) (2007) 2443–2450.

[79] H. Yang, K. Zhang, R. Shi, Sol–gel synthesis and photocatalytic activity of $CeO_2$/$TiO_2$ nanocomposites, J. Am. Ceram. Soc. 90 (5) (2007) 1370–1374.

[80] E. Setiawati, K. Kawano, Stabilization of anatase phase in the rare earth; Eu and Sm ion doped nanoparticle $TiO_2$, J. Alloys Compd. 451 (2008) 293–296.

[81] Lj.D. Arsov, C. Kormann, W. Plieth, Electrochemical synthesis and *in situ* Raman spectroscopy of thin films of titanium dioxide, J. Raman Spectrosc. 22 (10) (1991) 573–575.

[82] O. Toshiaki, I. Fujio, F. Yoshinori, Raman spectrum of anatase $TiO_2$, J. Raman Spectrosc. 7 (6) (1978) 321–324.
[83] W.F. Zhang, M.S. Zhang, Z. Yin, Q. Chen, Photoluminescence in anatase titanium dioxide nanocrystals, Appl. Phys. B: Lasers Opt. 70 (2) (2000) 261–265.
[84] J. Liqiang, S. Xiaojun, C. Weimin, X. Zili, D. Yaoguo, F. Honggang, The preparation and characterization of nanoparticle $TiO_2$/Ti films and their photocatalytic activity, J. Phys. Chem. Solid 64 (4) (2003) 615–623.
[85] U. Diebold, The surface science of titanium dioxide, Surf. Sci. Rep. 48 (2003) 53–229.
[86] M. Watanabe, T. Hayashi, Time-resolved study of self-trapped exciton luminescence in anatase $TiO_2$ under two-photon excitation, J. Lumin. 112 (2005) 88–91.
[87] I. Sildos, A. Suisalu, J. Aarik, T. Sekiya, S. Kurita, Self-trapped exciton emission in crystalline anatase, J. Lumin. 87–89 (2000) 290–292.
[88] Z. Lide, M. Jimei, Nanomaterials and Nanostructure, Science Press, Beijing, 2001, p. 312.
[89] H. Tang, K. Prasad, R. Sanjines, P.E. Schmid, F. Lévy, Electrical and optical properties of $TiO_2$ anatase thin films, J. Appl. Phys. 75 (4) (1994) 2042–2047.
[90] A.K. Ghosh, F.G. Wakim, R.R. Addiss Jr., Photoelectronic Processes in Rutile, Phys. Rev. 184 (3) (1969) 979–988.
[91] M. Hirano, K. Date, Scandium-doped anatase ($TiO_2$) nanoparticles directly formed by hydrothermal crystallization, J. Am. Ceram. Soc. 88 (2005) 2604–2607.
[92] J. Ovenstone, P.J. Titler, R. Withnall, J. Silver, A study of the effects of europium doping and calcination on the luminescence of titania phosphor materials, J. Phys. Chem. B 105 (30) (2001) 7170–7177.
[93] P.A. Tanner, L. Fu, B.-M. Cheng, Spectral band shifts in the electronic spectra of rare earth sesquioxide nanomaterials doped with europium, J. Phys. Chem. C 113 (2009) 10773–10779.
[94] M. Daldosso, D. Falcomer, A. Speghini, P. Ghigna, M. Bettinelli, Synthesis, EXAFS investigation and optical spectroscopy of nanocrystalline $Gd_3Ga_5O_{12}$ doped with $Ln^{3+}$ ions (Ln = Eu, Pr), Opt. Mater. 30 (7) (2008) 1162–1167.
[95] E.W.J.L. Oomen, A.M.A. van Dongen, Europium(III) in oxide glasses: dependence of the emission spectrum upon glass composition, J. Non-Cryst. Solids 111 (2/3) (1989) 205–213.
[96] K. Nakane, K. Yasuda, T. Ogihara, N. Ogata, S. Yamaguchi, Formation of poly(vinyl alcohol)–titanium lactate hybrid nanofibers and properties of $TiO_2$ nanofibers obtained by calcination of the hybrids, J. Appl. Polym. Sci. 104 (2) (2007) 1232–1235.
[97] J.-G. Li, X. Wang, K. Watanabe, T. Ishigaki, Phase structure and luminescence properties of $Eu^{3+}$-doped $TiO_2$ nanocrystals synthesized by $Ar/O_2$ radio frequency thermal plasma oxidation of liquid precursor mists, J. Phys. Chem. B 110 (3) (2006) 1121–1127.
[98] D. Falcomer, M. Daldosso, C. Cannas, A. Musinu, B. Lasio, S. Enzo, A. Speghini, M. Bettinelli, A one-step solvothermal route for the synthesis of nanocrystalline anatase $TiO_2$ doped with lanthanide ions, J. Solid State Chem. 179 (2006) 2452–2457.
[99] R.D. Peacock, The intensities of lanthanide $f \leftrightarrow f$ transitions, Struct. Bond. 22 (1975) 83–122.